



OPEN

Dynamic changes in immune cells in humanized liver metastasis and subcutaneous xenograft mouse models

Hyun Jin Bang^{1,4}, Kyung-Hwa Lee^{2,4}, Myong Suk Park¹, Eun-Gene Sun¹, Sang Hee Cho¹, Ik-Joo Chung^{1,3}, Hyun-Jeong Shim¹✉ & Woo Kyun Bae^{1,3}✉

Preclinical drug efficacy and tumor microenvironment (TME) investigations often utilize humanized xenograft mouse models, yet these models typically fall short in replicating the intricate TME. We developed a humanized liver metastasis (LM) model by transplanting human peripheral blood mononuclear cells (PBMCs) and assessed it against the conventional subcutaneous (SC) xenograft model, focusing on immune cell dynamics post-transplantation and immunotherapy response. NOD-*scid* IL2Rgamma^{null} (NSG) were inoculated with PBMCs to create humanized models. We induced SC and LM models using HCT116 cells, to investigate and compare the distributions and transformations of immune cell subsets, respectively. Both models were subjected to anti-PD-L1 therapy, followed by an analysis the TME analysis. The LM model demonstrated enhanced central tumor infiltration by tumor-infiltrating lymphocytes (TILs) compared to the peripheral pattern of SC model. TIL subpopulations in the LM model showed a progressive increase, contrasting with an initial rise and subsequent decline in the SC model. Post-anti-PD-L1 therapy, the LM model exhibited a significant rise in central and effector memory T cells, a response absent in the SC model. Our study highlights differential TME responses between SC and LM models and introduces a robust humanized LM model that swiftly indicates the potential efficacy of immunotherapies. These insights could streamline the preclinical evaluation of TME-targeting immunotherapeutic agents.

Xenograft mouse models have been used to evaluate the efficacy of preclinical drugs and to investigate the tumor microenvironment (TME). Xenograft mouse models have been developed via transplantation of human cancer cell lines or patient-derived cancer tissues into immune-deficient mice. In general, subcutaneous models (SC models) support translational research because they have the advantage of being easy to establish. However, SC models are primarily utilized to investigate local infiltration and are infrequently employed to study distant metastasis; moreover, they may not fully replicate the TME, potentially leading to tumorigenic mechanisms that differ from those observed in human cancers. To overcome these limitations, an experimental liver metastasis model (LM model) was developed via splenic injection or portal vein injection of tumor cells. Tumors in the LM model exhibit other properties, unlike those in the SC model¹. In addition, genetically engineered mouse models (GEMMs) more accurately simulate tumorigenesis and the TME, but the implementation of a humanized TME in these models is still challenging due to the murine immune system². Furthermore, GEMMs are not only complicated and time-consuming to develop but also established via varying methods³.

The importance of the TME has been established. Although xenograft models of metastasis have been well defined in mice, these models do not fully mimic the TME, which mainly consists of fibroblasts, endothelial cells, and immune cells that mediate tumor heterogeneity and complexity and support tumor growth⁴. Furthermore, tumor cells interact with the surrounding stromal tissues and immune cells, which can lead to tumor growth and

¹Division of Hematology-Oncology, Department of Internal Medicine, Chonnam National University Medical School and Hwasun Hospital, 322 Seoyang-Ro, Hwasun-Eup, Hwasun-Gun, Jeollanam-Do 58128, Republic of Korea. ²Department of Pathology, Bio-Medical Sciences Graduate Program (BMSGP), Chonnam National University Research Institute of Medical Science, Chonnam National University Medical School and Hwasun Hospital, Hwasun, Republic of Korea. ³Immunotherapy Innovation Center, Chonnam National University Medical School and Hwasun Hospital, Hwasun, Republic of Korea. ⁴These authors contributed equally: Hyun Jin Bang and Kyung-Hwa Lee. ✉email: hjihj@jnu.ac.kr; drwookyun@jnu.ac.kr

metastasis, as well as adaptive immune resistance⁵. To develop an optimized model, several attempts to reconstitute genes or factors from the environment surrounding the tumor have been made, but these approaches have been insufficient to accurately mimic the TME⁶. Immune cells have emerged as important components of the TME, and several humanized models involving the immune system have been developed to facilitate investigations of the efficacy of immunotherapies⁷. The goal of developing a humanized mouse model is to generate a TME with a fully human immune system that can be used to characterize the therapeutic response to immunotherapy. Different humanized mouse models have been engrafted with peripheral blood mononuclear cells (PBMCs), hematopoietic stem cells (HSCs), human fetal bone marrow (BM), liver tissue, thymic tissue, and splenic mononuclear cells. Although the PBMC-engrafted model lacks human B cells and human cytokines, it can be easily applied as a humanized mouse model because it is technically straightforward and can be established quickly⁸. This approach can be especially helpful for predicting the therapeutic outcomes of patient-specific immunotherapies using patient-derived xenograft (PDX) models for cancer patients who require a faster response than that achieved using other models.

In this study, we established a humanized LM mouse model through the transplantation of human PBMCs and conducted a comparative analysis of SC and LM models. Specifically, we examined the alterations in immune cell infiltration following transplantation and response to immunotherapy. Additionally, we explored factors that should be considered when employing these models in preclinical studies of cancer immunotherapy.

Results

Comparison of day 3 and day 7 in the LM model

To establish the humanized mouse LM model, 1×10^7 human fresh PBMCs were transplanted i.v. by injection following implantation of the HCT116 cell line. We attempted to optimize the humanized mouse LM model by comparing different time points of PBMC transplantation: day 3 (D3 model) and day 7 (D7 model). After comparing the D3 and D7 models, we observed that significantly fewer liver metastases had formed on D3 than on D7 by gross surgical examination, with a reduced metastatic burden ($p < 0.05$) and a reduced liver/body weight ratio ($p < 0.05$) (Fig. 1A–C). The mean values of liver metastatic burden were found to be 95.5% in the control group, 54.2% in the D3 model, and 81.8% in the D7 model. However, there were no differences in tumor burden and liver/body weight between the D7 model and mice that were not subjected to PBMC transplantation. The forward scatter and side scatter parameters in flow cytometry analysis were used to sort the immune cells in the blood and the liver on D3 and D7. Immune cells were observed following intracellular immunostaining with a human antibody panel that included human leukocytes (CD 45⁺), all T cells (CD45⁺CD3⁺), helper T cells (CD45⁺CD3⁺CD4⁺CD8⁻), cytotoxic T cells (CD45⁺CD3⁺CD4⁻CD8⁺), B cells (CD45⁺CD3⁻CD19⁺), and monocytes (CD45⁺CD14⁺). As shown in Fig. 1D and E, the proportions of total T cells, helper T cells, cytotoxic T cells, and B cells within the blood and liver were significantly greater on D3 than on D7. In addition, we analyzed the plasma levels of human TGF- β (hTGF- β) and human IFN- γ (hIFN- γ) after lymphocyte transplantation using ELISA. The hTGF- β plasma levels were lower in the D3 model than in the D7 model, whereas hIFN- γ plasma levels were higher in the D3 model than in the D7 model (Supplementary Fig. S1).

We observed that PBMC transplantation on day 3 increased the intensity of immune cell staining, and it could be used to optimize a humanized mouse LM model.

Immunologic characteristics: a comparative analysis of TME and cytokine profiles in SC and LM models

To explore whether the SC and LM models exhibit different tumor growth patterns, we examined both models concomitantly in the presence or absence of PBMC transplantation. After transplantation of PBMCs, both models exhibited attenuated tumor growth by gross observation, reduced tumor volume ($p < 0.05$), and a reduced tumor/body weight (BW) ratio ($p < 0.05$) compared with mice that were not subjected to PBMC transplantation (Fig. 2A–D). We conducted standard hematoxylin and eosin (H&E) staining and immunohistochemical staining (IHC) assays to verify the distribution of TILs in both models. Representative H&E and IHC images demonstrate infiltration of CD3⁺ Pan T-cells, CD8⁺ cytotoxic T-cells, and CD 4⁺ helper T-cells following PBMC transplantation, as shown in Fig. 2E and F. The infiltration of CD3⁺ T cells, CD8⁺ T cells, and CD 4⁺ T cells into the tumor was notably more pronounced and concentrated in the LM model. In contrast, Pan-B cells, NK cells, and macrophages were not observed in either model (Supplementary Fig. S2). To investigate the cytokines, we measured plasma hIFN- γ and hTGF- β levels. Plasma hIFN- γ levels were significantly increased after PBMC transplantation in both models ($p < 0.05$, Supplementary Fig. S3). In the SC model, hIFN- γ shows a continuous increase, whereas in the LM model, it decreases at the day 28. This decrease in the LM model is likely due to advanced cancer progression reaching a terminal stage, where the tumor can no longer grow. While the plasma levels of hTGF- β showed a different tendency than expected (Supplementary Fig. S3). In the SC model, there was no difference in hTGF- β levels according to PBMC transplantation until day 7, but after day 14, hTGF- β levels decreased significantly in the PBMC transplantation group ($p < 0.05$). The cancer progression is inhibited, which may lead to a decrease in hTGF- β levels. Conversely, hTGF- β levels in the LM model increased up to day 14, but after day 21, hTGF- β levels decreased in both groups and were significantly higher in those receiving PBMC transplantation.

These data indicate that PBMC transplantation resulted in T-cell proliferation, which inhibited tumor growth, in both the SC and LM models; in particular, central infiltration was observed in the LM model.

Comparative analysis of T cell number changes between the SC and LM models

We used several panels of human leukocyte markers in a flow cytometry assay to analyze the dynamic changes in T cell numbers in each model (Fig. 3). Overall, the total T cell population was increased in both models, and

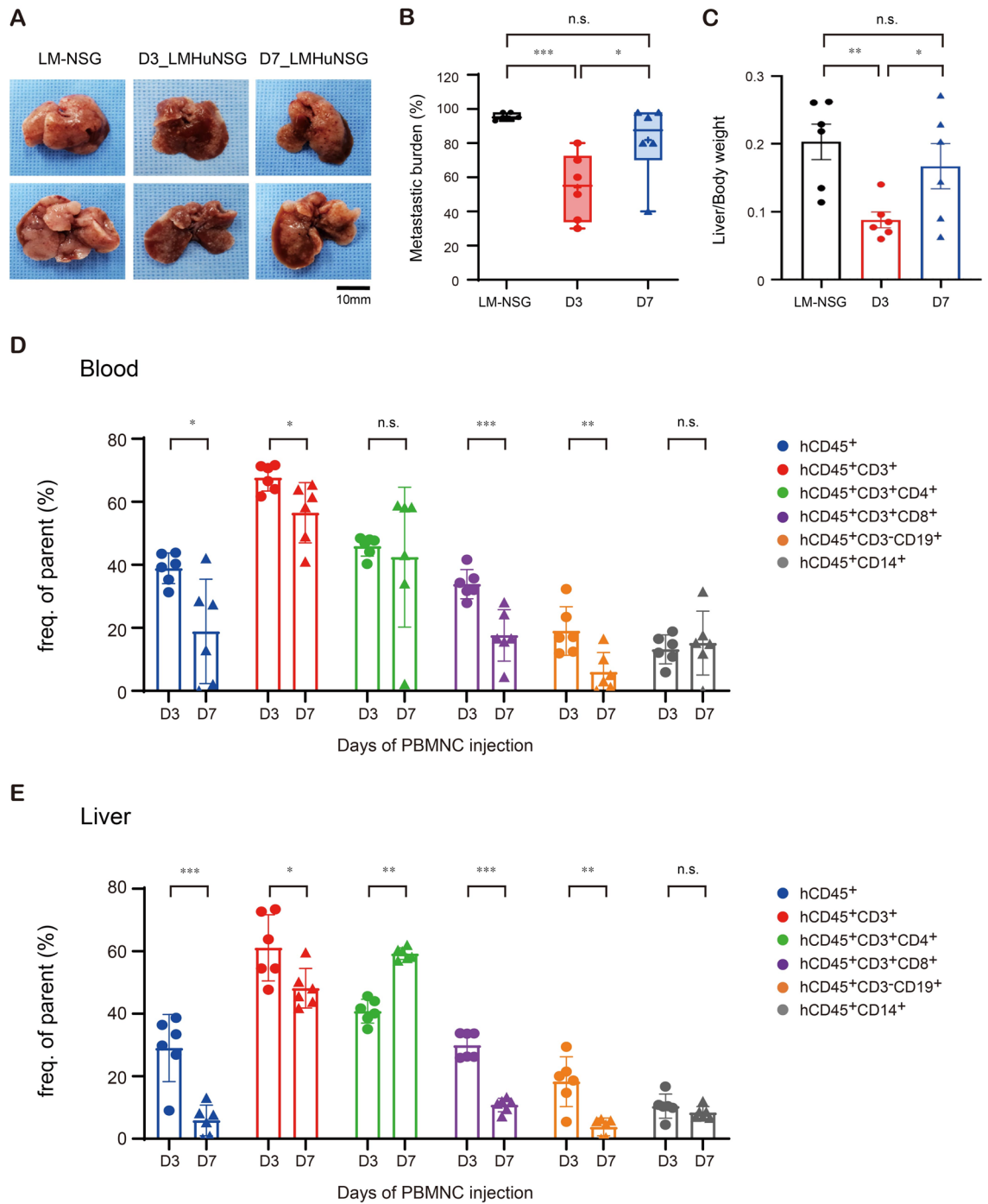


Figure 1. Establishment of a humanized liver metastasis mouse model via transplantation of peripheral blood mononuclear cells. **(A)** Representative images of the liver. **(B)** Metastatic burden and **(C)** quantification of liver weight in the liver metastatic (LM) model. **(D)** and **(E)** The percentages of human leukocytes (CD45⁺), total T cells (CD45⁺CD3⁺), helper T cells (CD45⁺CD3⁺CD4⁺), and cytotoxic T cells (CD45⁺CD3⁺CD8⁺) were analyzed in blood and liver samples. The circle indicates PBMC transplantation on day 3, and the triangle indicates day 7. The percentages of human leukocytes (CD45⁺), total T cells (CD45⁺CD3⁺), helper T cells (CD45⁺CD3⁺CD4⁺), and cytotoxic T cells (CD45⁺CD3⁺CD8⁺) were analyzed in the blood and liver (human PBMCs were injected i.v. on day 3 after intrasplenic injection). Mice of the male 5–6 week-old NOD-*scid* IL2Rgamma^{null}(NSG) mice as those in the experimental group (n = 6 mice per group) were used as normal controls. All mice were sacrificed on day 21 after intrasplenic injection of tumor cells. Error bars indicate SEM. n.s. not significant; **p* < 0.05; ***p* < 0.01; ****p* < 0.001; PBMC, peripheral blood mononuclear cell; LM-NSG, liver metastasis-NOD SCID gamma mouse; D3 model, PBMC transplantation on day 3 with liver metastasis model; D7 model, PBMC transplantation on day 7 with liver metastasis model, D3, PBMC transplantation on day 3 with liver metastasis model; D7, PBMC transplantation on day 7 with liver metastasis model.

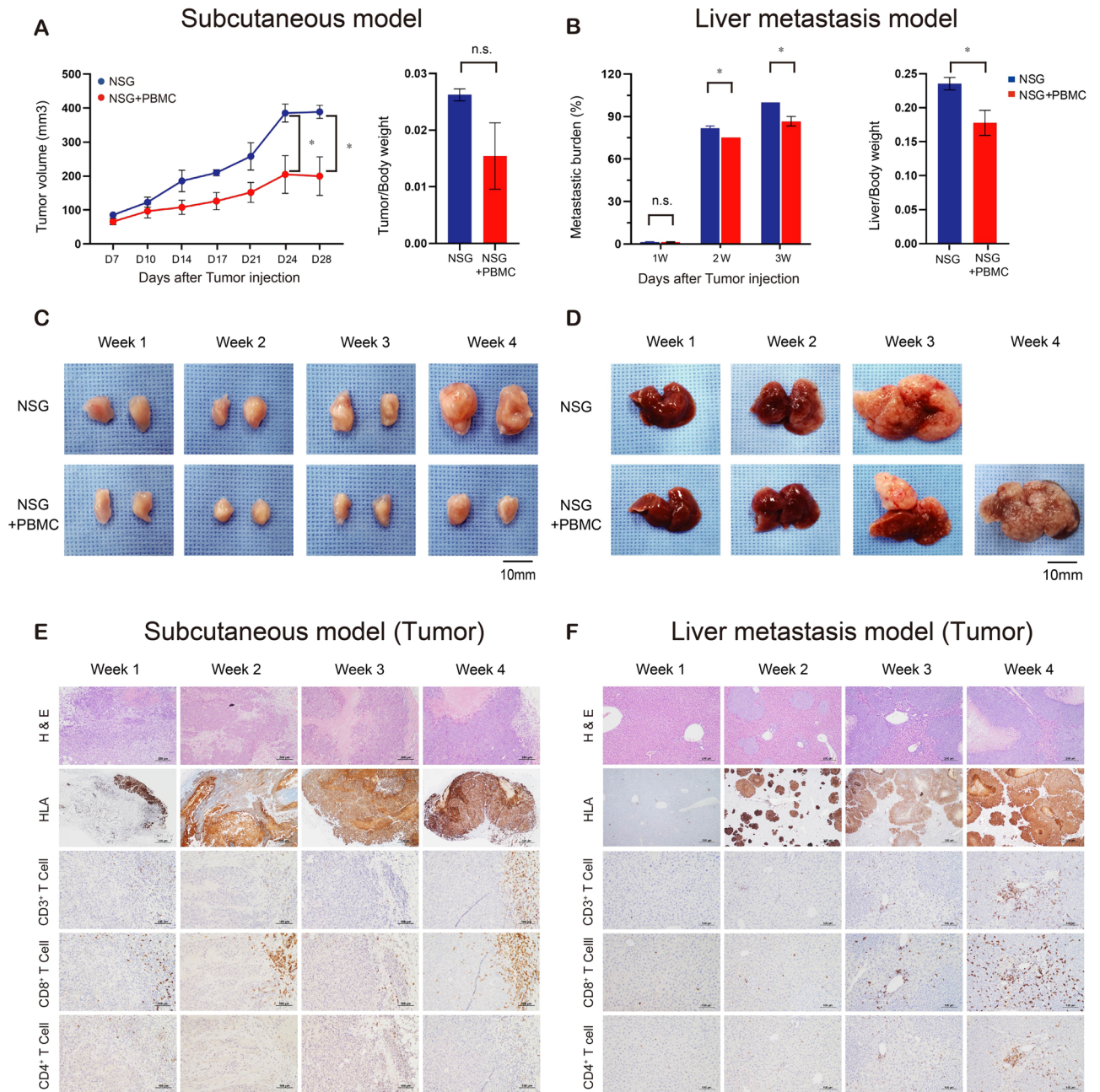


Figure 2. Analysis of tumor growth in a humanized mouse model via transplantation of peripheral blood mononuclear cells on day3. (A) Quantification of tumor growth and tumor weight in the subcutaneous (SC) model (B) and the liver metastasis (LM) model. (C) Representative images of tumors in the subcutaneous (SC) model. (D) LM model. (E) Histological analysis after hematoxylin and eosin (H&E) staining of CD3⁺T cells, CD4⁺ T cells, and CD8⁺ T cells in the SC model and (F) the LM model. Mice of the same sex and age as those in the experimental group were used as controls (n=5 mice per group). Tumor and liver tissues were collected every week after subcutaneous and intrasplenic injections and processed for histologic examination (×200). Error bars indicate the SEM. n.s. not significant; **p* < 0.05; PBMC, peripheral blood mononuclear cell; NSG, NOD SCID gamma mouse; NSG + PBMC, PBMC transplantation with NSG mouse; HLA, human leukocyte antigen; H & E, hematoxylin and eosin.

T cell numbers peaked on day 28 in the SC and LM models. T cell distribution, frequencies and proliferations in tumors were quantified using flow cytometry with specific marker panels to elucidate the kinetics of T cell changes in each humanized mouse model. In the SC model, hCD4⁺ T cell numbers increased and hCD4⁺Foxp3⁺ T cell numbers decreased. In contrast, hCD4⁺Foxp3⁺ T cell numbers were increased and hCD4⁺ cell numbers were decreased in the LM model. This indicates that tumor immune evasion and adaptation differ between the SC and LM models. We also detected hCD8⁺ IFN- γ ⁺ T cells, which showed an increasing tendency in the LM model, but we did not observe a similar tendency for hCD8⁺IFN- γ ⁺ T cells in the SC model. To further investigate

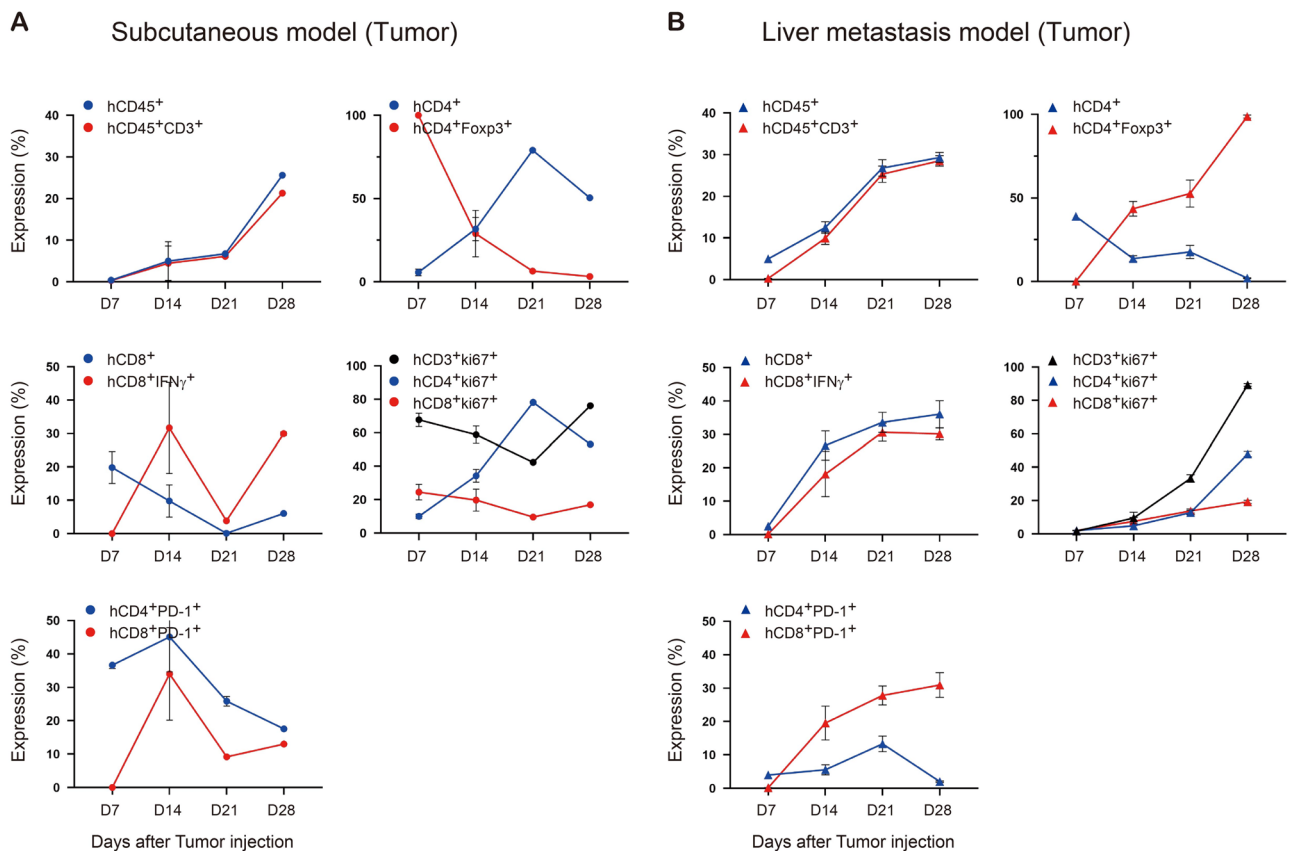


Figure 3. The kinetics of human immune cell changes in tumor tissue in the humanized mouse model. (A) Subcutaneous (SC) model. (B) Liver metastasis (LM) model. Tumor immune cell frequencies and absolute numbers in the SC model ($n=5$) and LM model ($n=5$) were analyzed every week by flow cytometry using the following phenotypes: human CD45⁺ (hCD45⁺), hCD45⁺hCD3⁺, hCD45⁺hCD3⁺hCD4⁺, hCD45⁺hCD3⁺hCD8⁺, hCD3⁺hCD4⁺hCD25⁺Foxp3⁺, hCD3⁺hCD8⁺IFN- γ ⁺, hCD3⁺Ki67⁺, hCD4⁺Ki67⁺, hCD8⁺Ki67⁺, hCD4⁺PD-1⁺ (hCD4⁺hCD274⁺), hCD8⁺PD-1⁺ (hCD8⁺hCD274⁺). Mice of the same sex and age as those in the experimental group were used as controls ($n=5$ mice per group). Tumor-infiltrating lymphocytes (TILs) from each treatment group were studied by flow cytometry every week after subcutaneous and intrasplenic injections.

the changes in cell populations and the proliferation of human T cells in humanized mice, we evaluated Ki-67 expression. In the SC model, hCD4⁺Ki67⁺ T cell numbers peaked at week 21, while hCD3⁺Ki67⁺ T cells and hCD8⁺Ki67⁺ T cell numbers remained at relatively low levels until week 21, before peaking at week 28. In the LM model, hCD3⁺Ki67⁺, hCD4⁺Ki67⁺, and hCD8⁺Ki67⁺ T cell numbers gradually increased and peaked at 28 weeks. When PD-1 expression in hCD4⁺ T cell and hCD8⁺ T cells was compared between the SC and LM models, PD-1-positive cell numbers in the SC model were found to peak at week 14 and then decrease. In contrast, in the LM model, hCD8⁺PD-1⁺ T cell numbers increased and peaked in week 28. We also examined T cells in the blood and found a pattern similar to that observed for tumor infiltration, but the peak was observed a week earlier than the peak of T cell numbers in the tumor (Supplementary Fig. S4). Notably, when the expression of PD-1 in hCD4⁺ and hCD8⁺ T cells was compared between the SC and LM models, PD-1 expression increased gradually in the LM model. Overall, in the LM model, regulatory T-cell and cytotoxic T-cell numbers increased, and proliferation and PD-1 expression also increased.

Comparison of the immunologic characteristics in the TME changes between SC and LM models following anti-PD-L1 therapy

We examined whether anti-PD-L1 therapy was effective in our humanized SC and LM mouse models. The experimental protocol used is outlined in Fig. 4A and B. In this experiment, we observed a decrease in PD-1 expression on day 14 in the SC model and day 21 in the LM model. Atezolizumab, an anti-PD-L1 inhibitor, was injected into the humanized SC and LM mouse models from day 7 to assess the efficacy of the drug against tumors, followed by administration of the same doses on days 14 and 21. As shown in Fig. 4C and D, atezolizumab reduced gross tumor volume and metastatic burden in both models, and this difference was significant in the LM model ($p < 0.05$). To further explore the profile of tumor-infiltrating lymphocytes (TILs) following treatment with atezolizumab, we performed H&E staining, image analysis by used ZEN Blue Software, and IHC analysis on tumor specimens from both models. First, significant differences in the number of TILs were observed in both models after treatment with atezolizumab, with observed increases in the numbers of pan T cells, helper T cells, cytotoxic T cells, and effector T cells (Fig. 4F,H) by ZEN Blue Software. Notably, in the SC

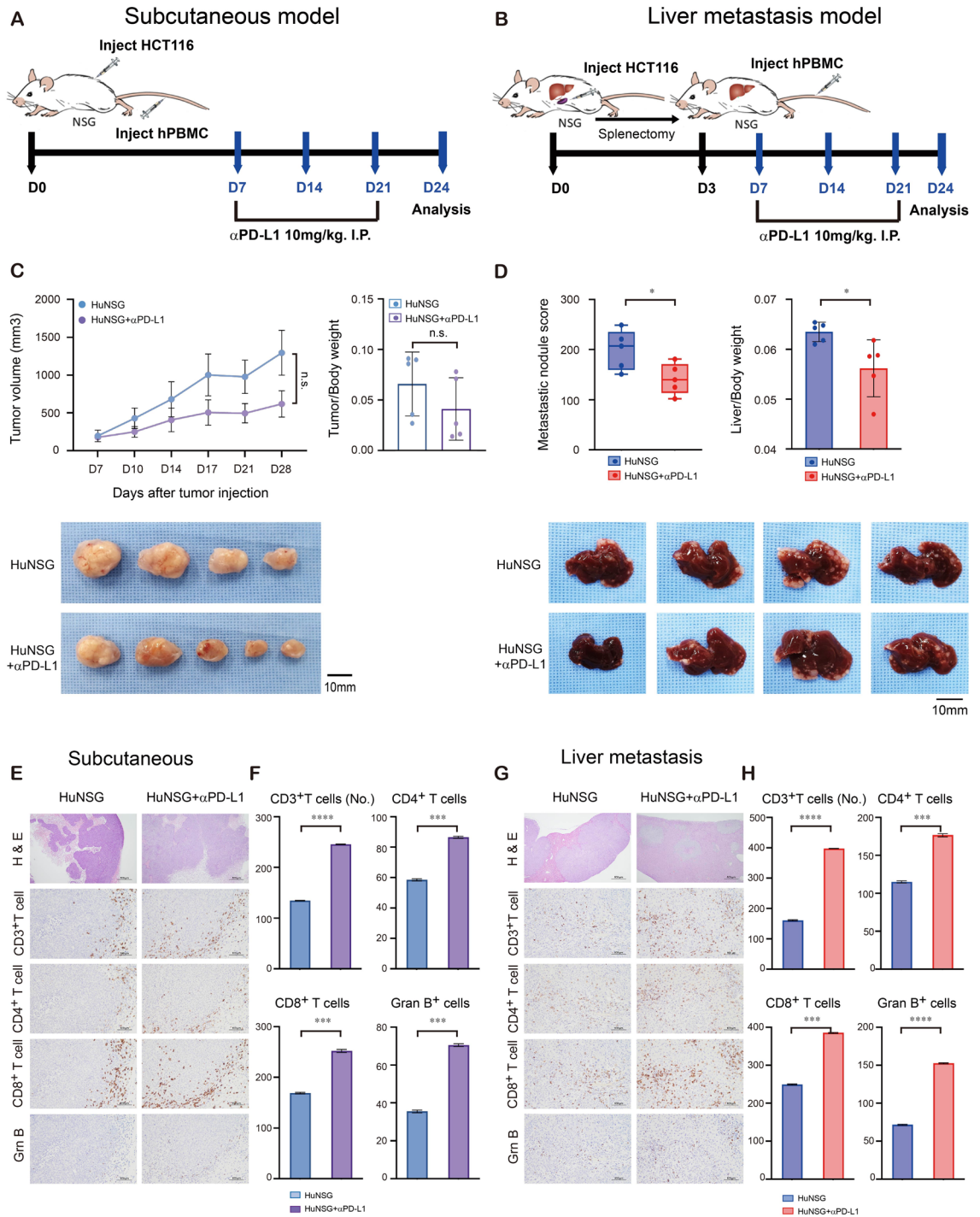


Figure 4. Schematic and histological analysis of anti-PD-L1 therapy in the humanized mouse models. **(A)** Subcutaneous model (SC model). **(B)** Liver metastasis model (LM model). **(C)** Representative images of tumor growth and quantification of tumor weight in the SC model and **(D)** the LM model. **(E)** Histological analysis of hematoxylin and eosin (H&E) staining and CD3⁺ T cells, CD4⁺ T cells, CD8⁺ T cells, and Granzyme B⁺ cells in the SC model and **(G)** the LM model. **(F)** Statistical analysis of human immune cells in tumors by ZEN Blue Software image analysis for the SC model and **(H)** the LM model. Mice of the same sex and age as those in the experimental group were used as controls (n = 5 mice per group). Tumor and liver tissues were collected every week after subcutaneous and intrasplenic injections and processed for histologic examination (×200) and ZEN Blue Software image analysis. Error bars indicate the SEM. n.s. not significant; *p < 0.05; **p < 0.01; ***p < 0.001; ****p < 0.0001; NSG, NOD SCID gamma mouse; HuNSG, peripheral blood mononuclear cell (PBMC) transplantation with NSG mouse; HuNSG + αPD-L1, anti-PD-L1 therapy was injected into the PBMC transplantation with NSG mouse; H & E, hematoxylin and eosin.

model, we found that most TILs were scattered around the tumor margin, whereas in the LM model, most TILs infiltrated into the center of the tumor (Fig. 4E,G).

Our data suggest that there are variations in tumor response and the distribution of TILs between the SC and LM models following anti-PD-L1 therapy.

Analysis of T cell and cytokine changes in the SC and LM models after anti-PD-L1 therapy

We analyzed T cell subsets following exposure to anti-PD-L1 therapy in both models by flow cytometry (Fig. 5). $hCD8^+$ T cell numbers were significantly increased in the LM model treated with atezolizumab compared with the SC model. Next, we investigated the distribution of memory $hCD8^+$ T-cell subsets, specifically naïve T cells (TcNs, $hCD8^+hCD45RA^+hCCR7^+$), effector T cells (TcEs, $hCD8^+hCD45RA^+hCCR7^-$), central memory T cells (TcCMs, $hCD8^+hCD45RA^+hCCR7^+$), and effector memory T cells (TcEMs, $hCD8^+hCD45RA^+hCCR7^-$). We observed that in the LM model, the numbers and sizes of the TcCM and TcEM populations were significantly increased by atezolizumab treatment. However, in the SC model, there were no significant changes observed. Furthermore, to evaluate the role of T cell differentiation and degranulation after anti-PD-L1 therapy, we analyzed individual cytolytic proteins in CD8 T cells that expressed $INF-\gamma^+$ and granzyme B. We observed a significant increase in $hCD8^+$ T cell differentiation and degranulation following treatment with atezolizumab in tumors in the LM model compared with the SC model. Furthermore, we observed that treatment with atezolizumab resulted in a significant decrease in $hCD4^+Foxp3^+$ T cell numbers in tumor tissues and blood samples from the LM model compared with those from the SC model.

To evaluate the functional activation of T lymphocytes after atezolizumab treatment in our humanized mouse model, we measured the concentrations of several human cytokines in plasma samples from both models. $hIFN-\gamma$, $hGranzyme B$, and $hTGF-\beta$ but not human tumor necrosis factor ($hTNF$) showed significant differences

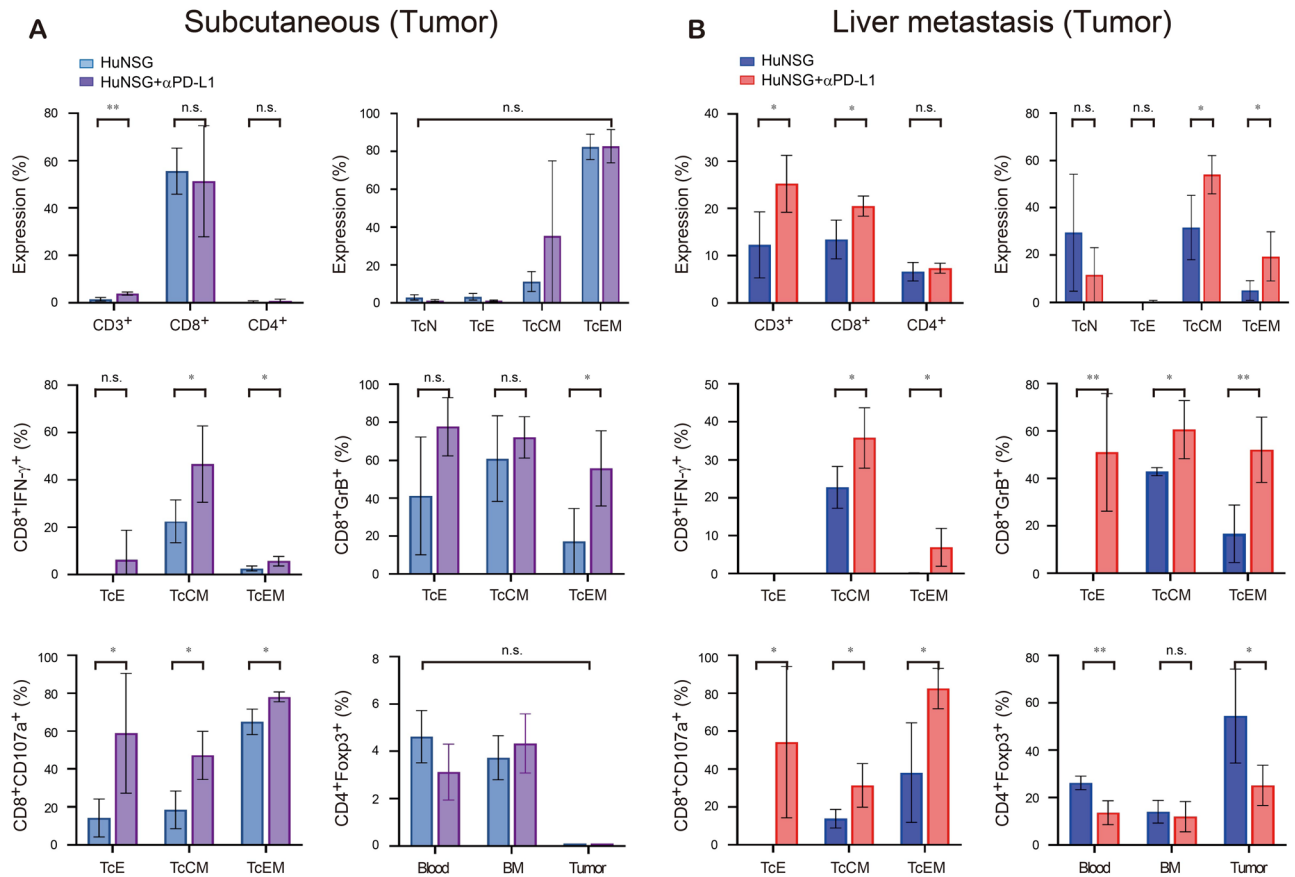


Figure 5. Statistical analysis of flow cytometry of immune cells after anti-PD-L1 therapy in the humanized mouse models on 24 days. (A) The subcutaneous (SC) model and (B) the liver metastasis (LM) model.

Tumor immune cell frequencies and absolute numbers in the SC model ($n = 5$) and LM model ($n = 5$) were analyzed by flow cytometry using the following phenotypes: human $CD45^+(hCD45^+)$, $hCD45^+hCD3^+$, $hCD45^+hCD3^+hCD4^+$, $hCD45^+hCD3^+hCD8^+$, $hCD3^+hCD4^+hCD25^+Foxp3^+$, $hCD3^+hCD8^+IFN-\gamma^+$, $hCD3^+hCD8^+Granzyme B^+$, $hCD3^+hCD8^+hCD107a^+$, TcN (Naïve T cell, $hCD8^+hCD45RA^+CCR7^+$), TcE (Effector T cell, $hCD8^+hCD45RA^+CCR7^-$), TcCM (Central memory T cell, $hCD8^+hCD45RA^+CCR7^+$), and TcEM (Effector memory T cell, $hCD8^+hCD45RA^+CCR7^-$). Error bars indicate the SEM. n.s. not significant; * $p < 0.05$; ** $p < 0.01$. HuNSG, peripheral blood mononuclear cell (PBMC) transplantation with NSG mouse; HuNSG + $\alpha PD-L1$, anti-PD-L1 therapy was injected into the PBMC transplantation with NSG mouse;

in SC model (Fig. 6). hTNE, hIFN- γ , and hGranzyme B levels were increased after atezolizumab treatment, while hTGF- β levels were decreased in LM model. In addition, hTGF- β levels were significantly reduced in the LM model compared to the SC model ($p < 0.001$).

Discussion

This study describes the development of a novel humanized mouse LM model using PBMCs. PBMC transplantation on day 3 was more suitable for developing a humanized mouse LM model than transplantation on day 7. Furthermore, we describe differences in the differentiation and proliferation of T cells between the SC and LM models, suggesting that the LM model is another mouse model that is suited for developing liver metastatic PDX tumor models for precision medicine, and provide evidence of modulation of the TME to achieve more effective immunotherapy.

A previous study demonstrated the efficacy of immunotherapy using a humanized mouse model through the application of PBMCs or HSCs and further extended that work to the development of the PDX model². A humanized mouse engrafted with human PBMCs or HSCs showed attenuated tumor growth, and when immunotherapy was administered, the tumor size decreased further⁷. Together, these results prompted the development of a PDX model to investigate the benefits of immunotherapy, with the primary aim of predicting the efficacy of therapy for cancer patients^{9–12}. However, in most studies except for some breast cancer studies, tumor cells were injected subcutaneously in humanized mouse models, which is insufficient to mimic the organ-specific TME^{13–16}. Zheng et al.¹⁶ showed that nivolumab inhibited osteosarcoma metastasis to the lung in humanized mice but did not affect the growth of the primary tumor, suggesting that the efficiency of immunotherapy may be organ specific. Although HSC transplantation can repopulate T cells, B cells, NK cells, DCs, and MDSCs, it does not allow the development of mature human immune cells prior to four weeks, which can be a considerable time delay for cancer patients. TGF- β is a well know cytokine that synthesized by tumor cells, endothelial cells, mesenchymal stem cells, cancer-associated fibroblasts, and macrophages, and it is related to tumor growth¹⁷. In our study, we use the cancer cells implanted in mice are HCT 116 cells, which are human colon cancer cells. And we can observe hTGF- β and hIFN- γ in both the humanized SC model and LM model that we developed. Notably, on D3, hTGF- β levels were found to be lower in the control arm compared to the D7 model. Conversely, hIFN- γ levels were higher in the D3 model compared to the other conditions. These findings suggest that for the development of a humanized LM model, transplanting PBMCs on D3 would be the most suitable approach for achieving optimal experimental outcomes. Here, we describe the development of a humanized liver metastasis mouse model using PBMCs that can be used to easily and quickly evaluate the preclinical efficacy of immunotherapies.

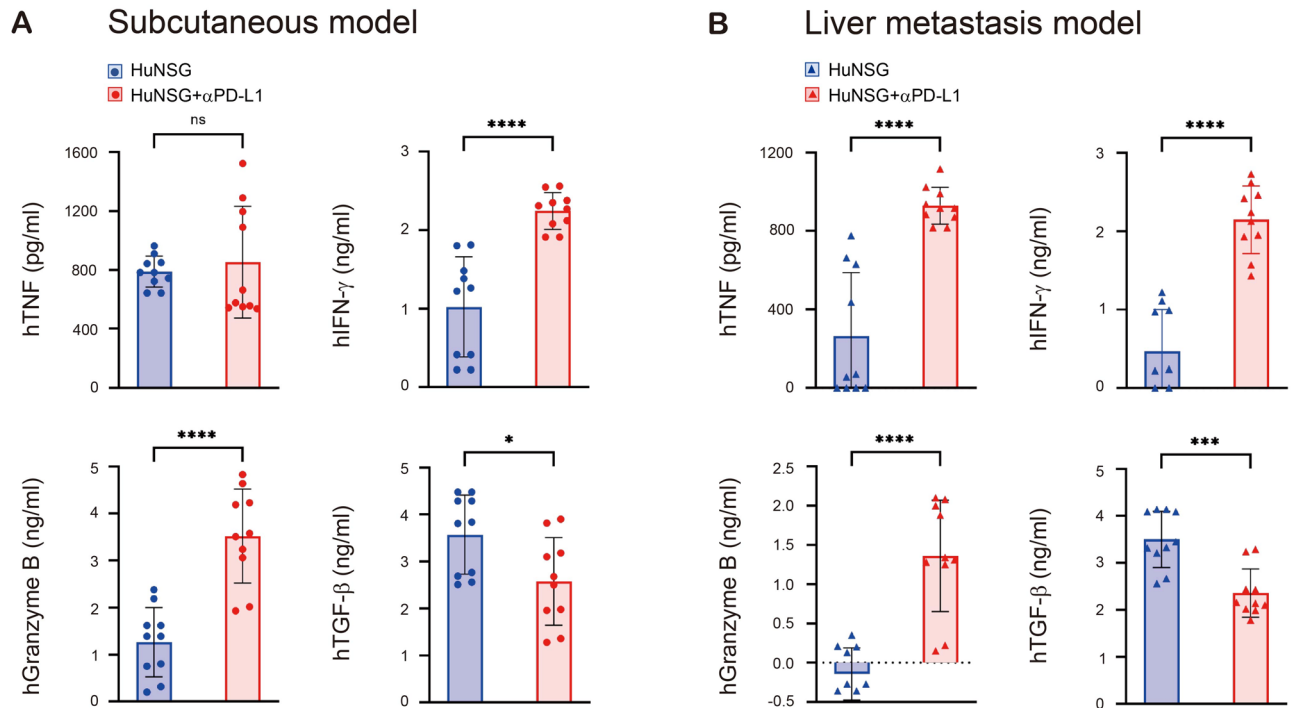


Figure 6. Analysis of human cytokine levels after anti-PD-L1 therapy in humanized mouse models. (A) Subcutaneous model. (B) Liver metastasis model. Serum samples were collected from humanized mice after 24 days by cardiac puncture under anesthesia. Cytokine quantification was performed using commercial ELISA kits for human IFN- γ (h IFN- γ), hGranzyme B, hTNF, and hTGF- β . All samples were measured in triplicate. Error bars indicate the SEM. n.s. not significant; * $p < 0.05$; ** $p < 0.01$; *** $p < 0.001$. HuNSG, peripheral blood mononuclear cell (PBMC) transplantation with NSG mouse; HuNSG + α PD-L1, anti-PD-L1 therapy was injected into the PBMC transplantation with NSG mouse; TNF, tumor necrosis factor.

Additionally, our study identified differences in the molecular profiles of T cell populations between the SC and LM models. In contrast to those in the SC model, cytotoxic T cell and regulatory T cell numbers increased in the humanized LM mouse model, and the overall proliferation of T cells also increased. Similarly, we found that the population of hCD8⁺PD1⁺ T cells increased in size in the LM model, whereas the populations of both hCD8⁺PD1⁺ and hCD4⁺PD1⁺ T cells decreased in size in the SC model. It is well known that immune cells within the TME stimulate and inhibit immune responses that can influence tumor growth⁴. Adaptive immune resistance in tumors involves the interaction between PD-1 and PD-L1 expressed on T cells and tumor cells, respectively, which mediates inhibitory signals¹⁸. Via ligation of PD-1 on T cells and PD-L1 on tumor cells, T-cell metabolism is altered, which leads to impaired activity of effector T cells and memory T cells and enhanced activity of regulatory T cells, which ultimately induces inhibitory signals in the TME⁵.

Tumor growth was significantly reduced following PD-L1 therapy in the developed humanized SC and LM models, and we observed differentiation of memory T cells in each model. In the LM model, both the central memory T cell and the effector memory T cell populations increased in size significantly compared to those in the SC model. To further investigate the levels of cytolytic proteins and degranulation in cytotoxic T cells, we evaluated the expression of markers of T-cell populations (hCD8⁺IFN- γ ⁺, hCD8⁺Granzyme B⁺, and hCD8⁺CD107a⁺). The expression of cytolytic proteins and the degranulation of T cells increased in both the SC and LM models after anti-PD-L1 therapy, which indicated that our humanized LM mouse model could also promote the propagation of memory T cells by achieving a high engraftment efficiency after anti-PD-L1 therapy, similar to the SC model. Interestingly, in patients who were treated with an anti-PD-1 blocking antibody, the numbers of memory T cells and effector T cells were increased in the TME, a finding that is correlated with a therapeutic response^{19–21}. However, despite treatment with immune checkpoint inhibitors that induce tumor cell death, tumor progression remains a concern that can be addressed by targeting the molecular and biochemical mechanisms of T cells.

Regarding the immunosuppressive effects of the TME, recent studies have shown that the modulation of regulatory T cells is important for changing the immunosuppressive activity of tumors^{22,23}. In particular, regulatory T cells (hCD4⁺Foxp3⁺) exhibited different outcomes after anti-PD-L1 therapy in the SC and LM models. In the SC model, we did not observe any notable responses of regulatory T cells in the blood and tumor tissues after anti-PD-L1 therapy, whereas in the LM model, we detected significant decreases in the numbers of regulatory T cells in the blood and tumor tissues. Overall, regulatory T cells could inhibit antitumor immunity, and early studies attempted to suppress the development of regulatory T cells in tumors. However, the suppression of effector T cell activity can occur through the elimination of regulatory T cells, mediated by signaling from various cytokines and chemokines within the TME²⁴. Therefore, it is crucial to concentrate on regulating the numbers and promoting the functional differentiation of regulatory T cells, effector T cells and memory T cells. Consequently, the development and characterization of humanized mouse tumor models are necessary for gaining a deeper insight into the dynamic alterations in T cells. These findings may unveil a novel anticancer function for T cells within the TME²⁵.

In addition to investigating the functional characteristics of immune cells in response to tumors, we should also consider differences in the organ-specific TME to better combat immunosuppressive tumors. The efficacy of immunotherapy has already been shown to vary depending on the type of cancer, but organ-specific responses to immunotherapy may also achieve discordant results due to the TME, a phenomenon that was discussed previously²⁶. In addition, in patients with advanced hepatocellular carcinoma, the effects of immunotherapy were observed to differ across organs such as the site of the primary tumor, the lung, and the liver²⁷. Thus, we need to concentrate on different organ-specific TMEs, and new treatment strategies should be developed based on insights from the observed resistance mechanisms, which may ultimately allow us to identify potential treatments for immunosuppressive tumors. Furthermore, different tumor implantation sites in the humanized mouse model provide information on the organ-specific roles of immune cells and may suggest approaches to overcome immune-resistant tumors. Colorectal cancer (CRC) is known to frequently metastasize to the liver due to the anatomical drainage via the portal vein²⁸. This study aims to establish a suitable animal model for future immunotherapy drug testing by using a liver metastasis model of CRC, wherein PBMCs are injected to create a human immune cell-engrafted model. Typically, to induce liver metastasis of CRC, cancer cells are transplanted into the colon wall of the cecum. However, this method is associated with issues of low predictability, reproducibility, and is time-consuming. In contrast, since the splenic vein is connected to the portal vein, injecting colon cancer cell lines into the spleen provides a method with high reproducibility and efficiency. This approach facilitates the timely development of a liver metastasis model, which is critical for the prompt completion of experiments prior to the onset of graft-versus-host disease (GVHD)²⁹. Through our novel approach using the developed humanized mouse model, we provide a comprehensive approach to developing a PDX model that closely mimics the functional immune system and stromal components of a patient.

One limitation of our study is that we did not examine the HLA mismatch between injected PBMCs and cancer cells. However, our experiments were conducted within 4 weeks, particularly before the onset of graft-versus-host disease (GVHD) resulting from HLA mismatch. Our LM model could still prove valuable for swiftly establishing PDX models for investigating novel treatments. Another limitation is our inability to detect B cells, NK T cells, or macrophages. While PBMC transplantation is suitable for validating the efficacy of anti-PD-L1 therapy in PDX models, refining the methods for HSC transplantation is necessary. This is crucial because an effective TME can be established by T cells, NK T cells, and B cells derived from HSCs, facilitating a deeper understanding of the specific mechanisms of underlying tumorigenesis.

In conclusion, our study compared a humanized mouse SC and LM model and demonstrated that differences between the two models in the proportions of cytotoxic T cells and regulatory T cells, along with the expression of PD-1 on the T cells, may contribute to the development of antitumor immunity, reflecting the impact of the reprogrammed TME in immune cells. Furthermore, we illustrated an antitumor response following atezolizumab treatment, attributed to a significant reduction in the proportion of regulatory T cells and increases in

the proportions of effector T cells and memory T cells. Our research highlighted notable differences in immune cells composition within the TME in humanized mouse models undergoing immunotherapy. These findings are expected to aid in further exploration of the role TME's role, enhancing our understanding of the efficacy of novel agents that modulate the immune microenvironment to achieve successful anticancer therapy.

Materials and methods

Cell lines

The HCT116 cell line was obtained from the American Type Culture Collection (ATCC, Manassas, VA, USA) and was maintained in McCoy's 5A medium (Invitrogen, Frederick, MD, USA) supplemented with 10% heat-inactivated fetal bovine serum (FBS), 100 U/mL penicillin and 100 µg/mL streptomycin. Cells were maintained in a humidified (37 °C, 5% CO₂) incubator and passaged when they reached 80% confluence. In this study, we conducted experiments using human colon cancer cell lines, HCT116 cells. Previously we reported many experiments using the HCT116 cells liver metastasis model^{30,31}.

Mice

NSG mice, which were established by backcrossing a null mutation of the *Il2ry* locus onto the NOD.Cg-Prkdc^{scid} (NOD/SCID) strain, were purchased from The Jackson Laboratory. The mice were sacrificed with isoflurane euthanasia within a month of the end of the study. Experiments involving NSG mice were performed according to the guidelines of the Chonnam National University Medical School Research Institutional Animal Care Committee, and all animal experimental protocols were approved by the Chonnam National University Medical School Research Institutional Animal and Use Committee (Gwangju, Republic of Korea, CNU IACUC-H-2022-31). Our study was confirmed by ARRIVE essential 10 guidelines 2.0³².

Subcutaneous model

To establish the experimental subcutaneous (SC) model, male 5- to 6-week-old NOD-*scid* IL2Rgamma^{null}(NSG) mice were injected intravenously (i.v.) with 1×10^7 human fresh PBMCs, and 3×10^6 HCT116 human colon carcinoma cells suspended in 100 µL of phosphate-buffered saline (PBS) were injected subcutaneously (s.c.) into the flank of the mice on day 0 of the experiment. Tumor growth was recorded every 3 to 4 days for 4 weeks. Mice were euthanized every week, and SC tumors were removed, weighed, and processed for histologic examination; cells collected from residual tumor tissue, blood, BM, and spleen cells were subjected to flow cytometry analysis.

Liver metastasis model

To establish the experimental liver metastasis (LM) model, HCT116 cells (2×10^6 cells/mouse) were injected into the spleen of the mice to induce colorectal liver metastasis¹. Splenectomy was performed 10 min after injecting HCT116 cells. The skin and peritoneum of the mice were sutured and used for colorectal liver metastasis studies. In our previous studies aimed at researching the liver metastasis model, we monitored the IVIS 200 Imaging system daily and have been reported^{33,34}. Based on these studies, we found that after performing splenectomy, the seeding and growth of cancer cells in the liver begin from day 2. After 3 days or 7 days, the mice were injected i.v. with 1×10^7 human fresh PBMCs. The weight of each mouse was recorded every 3–4 days for 4 weeks. Mice were euthanized weekly, and liver tissue was removed, weighed, and processed for histologic examination. Cells were collected from the liver and blood for flow cytometry analysis. The metastatic burden calculated by this method (Metastatic burden (%) = (tumor area)/(liver area) X 100). The whole liver area, which consists of the left lateral lobe, left and right medial lobes, and the caudate lobe, including both the front and back surfaces, was measured and summed. And the ratio of liver/body weight calculated by this method (Liver/Body weight ratio = Liver weight/Body weight).

Histologic examination and immunohistochemistry

The excised wound tissue was fixed in 10% neutral-buffered formalin and then dissected and embedded in paraffin. Tissue blocks were sectioned at a 3 µm thickness using a microtome and stained with hematoxylin and eosin (H&E). Unstained slides from each tissue block were immunostained with specific antibodies using a Bond-Max Autostainer (Leica Microsystems, Buffalo Grove, IL, USA). Antibodies against the following factors were used: CD7 (1:100 dilution; catalog no. M7255; DAKO, Glostrup, Denmark), CD4 (1:100 dilution; catalog no. NCL-L-CD4_368; Novocastra, Newcastle, UK), CD8 (ready to use; catalog no. PA0183; Novocastra), Granzyme B (1:50 dilution; catalog no. M7235; DAKO), CD79a (1:300 dilution; catalog no. 179 M-95; Cell Marque, Rocklin, CA, USA), CD56 (1:400 dilution; catalog no. M7304; DAKO), CD68 (1:100 dilution; catalog no. MO814; DAKO), and human leukocyte antigens (HLAs) (1:300 dilution; catalog no. ab70328; Abcam, Cambridge, UK). The slides were evaluated by an experienced pathologist (KHL) and photographed using the Nikon DS-Ri2 system (Nikon Japan, Tokyo, Japan). The images were processed using ZEN Blue Software.

Human peripheral blood mononuclear cells

All participants signed an ethical consent form approved by the Institutional Review Board of Chonnam National University Hwasun Hospital (Hwasun, Republic of Korea, CNUHH-2021–045). Human PBMCs were obtained from healthy volunteers and were isolated from blood samples by density-gradient centrifugation with Ficoll-Hypaque (d = 1.077 gm/mL, Lymphoprep™, Axis-Shield, Oslo, Norway, 1114545) and washed with PBS. NOD-*scid* IL2Rgamma^{null}(NSG) mice were injected i.v. with 1×10^7 human PBMCs suspended in 100 µL of normal saline.

Cell preparation

The mice were sacrificed with isoflurane euthanasia within a month of the end of the study, which is before developing graft-versus-host disease (GVHD)³⁵. Tumor was collected from the heart immediately following euthanasia, and serum was frozen in a -80 °C deep freezer for future analyses. Liver, lymph node (LN), spleen, and BM specimens were processed into single-cell suspensions. Tumors were extracted and weighed, and was fixed in 10% formalin (Core fix) for histological analyses. The remaining tumor sections were minced and digested using 4–8 mg of collagenase D (Roche) per tumor in PBS for 1.5–2 h at 37 °C³⁶. The liver was minced into 1-mm pieces and digested using collagenase IV for 30 min at 37 °C. The digested liver extract was filtered through a 70- μ m cell strainer and centrifuged at 500 \times g for 5 min. The resulting cell pellet was resuspended in 10 mL of 35% Percoll containing 100 U/mL heparin and centrifuged at 700 \times g for 15 min at room temperature. The cell pellet containing the leukocytes was collected and resuspended in 3 mL of red blood cell lysis solution (155 mM NH₄Cl, 10 mM KHCO₃, 1 mM EDTA, 170 mM Tris, pH 7.3). After incubation for 3 min on ice, the cells were washed twice in RPMI 1640 containing 5% FBS³⁷. The BM and spleen cells were prepared by standard methods and were incubated with ammonium chloride-potassium (ACK) lysis buffer (Life Technologies) for 10 min at room temperature with gentle mixing. For mice in which lymph nodes were not visible by the naked eye, small tissue samples from LN sites were processed for flow cytometry analyses to assess the presence of human lymphocytes.

Flow cytometry

For surface staining, cells were washed twice in fluorescence-activated cell sorting (FACS) buffer (1X PBS w/2% FBS, 1 mM EDTA, and 0.1% sodium azide), incubated with Fc blocking reagent (Miltenyi Biotec), and stained with fluorescence-conjugated antibodies in brilliant stain buffer (BD Horizon™, Catalog: 566349). For intracellular staining, cells were labeled with surface markers as previously described and then fixed and permeabilized with the Transcription Factor Buffer Set (BD Pharmingen™, Catalog: 554714). A 5-antibody panel was used for this study. The human T-cell panel (6 colors) consisted of mouse anti-human antibodies against CD45 (clone: HI30, catalog: 564105), CD3 (clone: UCHT1, catalog: 561807), CD4 (clone: RPA-T4, catalog: 561841), CD8 (clone: RPA-T8, catalog: 555367), CD274 (PD-1) (clone: EH12.1, catalog: 563076), and Ki-67 (clone: B56, catalog: 562899). The human B- and NK-cell panel (4 colors) consisted of CD45 (clone: HI30, catalog: 564105), CD3 (clone: UCHT1, catalog: 561807), CD19 (clone: HIB19, catalog: 562440), and CD56 (clone: CMSSB, catalog: 12–0567–42). The human macrophage panel (3 colors) consisted of CD45 (clone: HI30, catalog: 564105), CD68 (clone: Y1/82A, catalog: 562117), and CD11c (clone: GHI/61, catalog: 562670). The human regulatory T-cell panel (5 colors) consisted of CD45 (clone: HI30, catalog: 564105), CD3 (clone: HIT3a, catalog: 564713), CD4 (clone: RPA-T4, catalog: 561841), CD25 (clone: M-A251, catalog: 555431), and Foxp3 (clone: 236A/E7, catalog: 72–5774–40). The human cytotoxic T-cell panel (4 colors) consisted of CD45 (clone: HI30, catalog: 564105), CD3 (clone: UCHT1, catalog: 561807), CD8 (clone: RPA-T8, catalog: 555367), and IFN- γ (clone: B27, catalog: 554702). The human monocyte and dendritic cell (DC) panel (3 colors) consisted of CD45 (clone: HI30, catalog: 564105), CD14 (clone: M5E2, catalog: 561712), and CD11c (clone: -ly6, catalog: 562561), all purchased from BD Bioscience and eBioscience. The human cytotoxic T-cell panel (5 colors) consisted of CD3 (clone: UCHT1, catalog: 561807), CD4 (clone: RPA-T4, catalog: 557871), CD8 (clone: RPA-T8, catalog: 555367), CD45RA (clone: L48, catalog: 337186), and CCR7 (clone: 3D12, catalog: 560548). Human cytolytic proteins in cytotoxic T cells (8 colors) were stained with CD3 (clone: UCHT1, catalog: 561807), CD4 (clone: RPA-T4, catalog: 557871), CD8 (clone: RPA-T8, catalog: 555367), CD45RA (clone: L48, catalog: 337186), CCR7 (clone: 3D12, catalog: 560548), CD107a (clone: H4A3, catalog: 560664), IFN- γ (clone: B27, catalog: 554702), and granzyme B (clone: GB11, catalog: 563389). The cells were further permeabilized using the Fixation/Permeabilization Kit (BD Bioscience) and stained for Ki-67, CD68, Granzyme B, and INF- γ . For staining of Foxp3, cells were permeabilized using the anti-human Foxp3 staining Set-PE (eBioscience™). All cells were analyzed using a BD FACSCanto II flow cytometer (BD Biosciences) (Fig. S5, S6, S7, S8). The data were analyzed using FlowJo v10.6.2. software (BD Biosciences).

Measurement of in vivo release of human cytokines

Serum samples were collected from the humanized mice every week for 4 weeks by cardiac puncture under anesthesia. Cytokine quantification was performed using commercial ELISA kits for human IFN- γ (BD Bioscience, San Diego, CA, USA., 555142) and hIL-10 (BD Bioscience, San Diego, CA, USA., 555157), hTGF- β 1 (ELISA Duo-set; R&D Systems, Inc., Canada, USA., DY240-05), and Granzyme B (R&D Systems, Inc. Canada, USA., DY2906-05) according to the manufacturer's instructions. All samples were measured in triplicate, and the absorbance was read at 450 nm in an ELISA reader.

Statistical analysis

Data were analyzed using paired or unpaired t tests, and one-way ANOVA was performed to compare groups; a *p* value < 0.05 was considered to indicate statistical significance. All statistical analyses were performed using SPSS v.23.0 (IBM, Armonk, NY, USA) and/or GraphPad Prism v.9 software (GraphPad Software, San Diego, CA, USA).

Ethics approval

All animal protocols were approved by The Chonnam National University Medical School Research Institutional Animal Care and Use Committee.

Data availability

Data is provided within the manuscript or supplementary information files.

References

- Bae, K. B., Kim, S. H., Kang, M. S. & Kim, D. H. An animal model of colorectal cancer liver metastasis with a high metastasis rate and clonal dynamics. *Anticancer Res.* **40**, 3297–3306. <https://doi.org/10.21873/anticancer.14312> (2020).
- Olson, B., Li, Y., Lin, Y., Liu, E. T. & Patnaik, A. Mouse models for cancer immunotherapy research. *Cancer Discov.* **8**, 1358–1365. <https://doi.org/10.1158/2159-8290.CD-18-0044> (2018).
- Chulpanova, D. S., Kitaeva, K. V., Rutland, C. S., Rizvanov, A. A. & Solovyeva, V. V. Mouse tumor models for advanced cancer immunotherapy. *Int. J. Mol. Sci.* <https://doi.org/10.3390/ijms21114118> (2020).
- Junttila, M. R. & de Sauvage, F. J. Influence of tumour micro-environment heterogeneity on therapeutic response. *Nature* **501**, 346–354. <https://doi.org/10.1038/nature12626> (2013).
- Boussiotis, V. A. Molecular and biochemical aspects of the PD-1 checkpoint pathway. *N. Engl. J. Med.* **375**, 1767–1778. <https://doi.org/10.1056/NEJMra1514296> (2016).
- Zhang, Y. *et al.* Establishing metastatic patient-derived xenograft model for colorectal cancer. *Jpn. J. Clin. Oncol.* **50**, 1108–1116. <https://doi.org/10.1093/jjco/hyaa089> (2020).
- Wang, M. *et al.* Humanized mice in studying efficacy and mechanisms of PD-1-targeted cancer immunotherapy. *FASEB J.* **32**, 1537–1549. <https://doi.org/10.1096/fj.201700740R> (2018).
- Cogels, M. M. *et al.* Humanized mice as a valuable pre-clinical model for cancer immunotherapy research. *Front. Oncol.* **11**, 784947. <https://doi.org/10.3389/fonc.2021.784947> (2021).
- Baschnagel, A. M. *et al.* Development and characterization of patient-derived xenografts from non-small cell lung cancer brain metastases. *Sci. Rep.* **11**, 2520. <https://doi.org/10.1038/s41598-021-81832-1> (2021).
- Inoue, A. *et al.* Current and future horizons of patient-derived xenograft models in colorectal cancer translational research. *Cancers (Basel)* <https://doi.org/10.3390/cancers11091321> (2019).
- Xu, W. *et al.* Comprehensive comparison of patient-derived xenograft models in hepatocellular carcinoma and metastatic liver cancer. *Int. J. Med. Sci.* **17**, 3073–3081. <https://doi.org/10.7150/ijms.46686> (2020).
- Zitvogel, L., Pitt, J. M., Dailly, R., Smyth, M. J. & Kroemer, G. Mouse models in oncoimmunology. *Nat. Rev. Cancer* **16**, 759–773. <https://doi.org/10.1038/nrc.2016.91> (2016).
- Meraz, I. M. *et al.* An improved patient-derived xenograft humanized mouse model for evaluation of lung cancer immune responses. *Cancer Immunol. Res.* **7**, 1267–1279. <https://doi.org/10.1158/2326-6066.CIR-18-0874> (2019).
- Rosato, R. R. *et al.* Evaluation of anti-PD-1-based therapy against triple-negative breast cancer patient-derived xenograft tumors engrafted in humanized mouse models. *Breast Cancer Res.* **20**, 108. <https://doi.org/10.1186/s13058-018-1037-4> (2018).
- Sanmamed, M. F. *et al.* Nivolumab and urelumab enhance antitumor activity of human T Lymphocytes engrafted in Rag2-/-IL2Rgammanull immunodeficient mice. *Cancer Res.* **75**, 3466–3478. <https://doi.org/10.1158/0008-5472.CAN-14-3510> (2015).
- Zheng, B. *et al.* PD-1 axis expression in musculoskeletal tumors and antitumor effect of nivolumab in osteosarcoma model of humanized mouse. *J. Hematol. Oncol.* **11**, 16. <https://doi.org/10.1186/s13045-018-0560-1> (2018).
- Derynck, R., Turley, S. J. & Akhurst, R. J. TGF β biology in cancer progression and immunotherapy. *Nat. Rev. Clin. Oncol.* **18**, 9–34. <https://doi.org/10.1038/s41571-020-0403-1> (2021).
- Pardoll, D. M. The blockade of immune checkpoints in cancer immunotherapy. *Nat. Rev. Cancer* **12**, 252–264. <https://doi.org/10.1038/nrc3239> (2012).
- Han, J. *et al.* Resident and circulating memory T cells persist for years in melanoma patients with durable responses to immunotherapy. *Nat. Cancer* **2**, 300–311. <https://doi.org/10.1038/s43018-021-00180-1> (2021).
- Herbst, R. S. *et al.* Predictive correlates of response to the anti-PD-L1 antibody MPDL3280A in cancer patients. *Nature* **515**, 563–567. <https://doi.org/10.1038/nature14011> (2014).
- Ribas, A. *et al.* PD-1 blockade expands intratumoral memory T cells. *Cancer Immunol. Res.* **4**, 194–203. <https://doi.org/10.1158/2326-6066.CIR-15-0210> (2016).
- Chen, B. J., Zhao, J. W., Zhang, D. H., Zheng, A. H. & Wu, G. Q. Immunotherapy of cancer by targeting regulatory T cells. *Int. Immunopharmacol.* **104**, 108469. <https://doi.org/10.1016/j.intimp.2021.108469> (2022).
- Togashi, Y., Shitara, K. & Nishikawa, H. Regulatory T cells in cancer immunosuppression - implications for anticancer therapy. *Nat. Rev. Clin. Oncol.* **16**, 356–371. <https://doi.org/10.1038/s41571-019-0175-7> (2019).
- Li, C., Jiang, P., Wei, S., Xu, X. & Wang, J. Regulatory T cells in tumor microenvironment: new mechanisms, potential therapeutic strategies and future prospects. *Mol. Cancer* **19**, 116. <https://doi.org/10.1186/s12943-020-01234-1> (2020).
- Morton, J. J., Bird, G., Refaeli, Y. & Jimeno, A. Humanized mouse xenograft models: Narrowing the tumor-microenvironment gap. *Cancer Res.* **76**, 6153–6158. <https://doi.org/10.1158/0008-5472.CAN-16-1260> (2016).
- Conway, J. W. *et al.* The effect of organ-specific tumor microenvironments on response patterns to immunotherapy. *Front. Immunol.* **13**, 1030147. <https://doi.org/10.3389/fimmu.2022.1030147> (2022).
- Lu, L. C. *et al.* Differential organ-specific tumor response to immune checkpoint inhibitors in hepatocellular carcinoma. *Liver Cancer* **8**, 480–490. <https://doi.org/10.1159/000501275> (2019).
- Valderrama-Treviño, A. I., Barrera-Mera, B., Ceballos-Villalva, J. C. & Montalvo-Javé, E. E. Hepatic metastasis from colorectal cancer. *Euroasian J. Hepatogastroenterol.* **7**, 166–175. <https://doi.org/10.5005/jp-journals-10018-1241> (2017).
- Oh, B. Y., Hong, H. K., Lee, W. Y. & Cho, Y. B. Animal models of colorectal cancer with liver metastasis. *Cancer Lett.* **387**, 114–120. <https://doi.org/10.1016/j.canlet.2016.01.048> (2017).
- Bae, J. A. *et al.* A new KSRP-binding compound suppresses distant metastasis of colorectal cancer by targeting the oncogenic KITENIN complex. *Mol. Cancer* **20**, 78. <https://doi.org/10.1186/s12943-021-01368-w> (2021).
- Nguyen, H. P. Q. *et al.* Intensified NK cell therapy in combination with low-dose chemoradiotherapy against human colorectal cancer. *Cancer Immunol. Immunother.* **72**, 4089–4102. <https://doi.org/10.1007/s00262-023-03545-w> (2023).
- Percie du Sert, N. *et al.* Reporting animal research: Explanation and elaboration for the ARRIVE guidelines 2.0. *PLoS Biol.* **18**, e3000411. <https://doi.org/10.1371/journal.pbio.3000411> (2020).
- Kang, S. H. *et al.* Oral siRNA delivery to treat colorectal liver metastases. *ACS Nano* **11**, 10417–10429. <https://doi.org/10.1021/acsnano.7b05547> (2017).
- Yang, Y. *et al.* Potassium usnate, a water-soluble usnic acid salt, shows enhanced bioavailability and inhibits invasion and metastasis in colorectal cancer. *Sci. Rep.* **8**, 16234. <https://doi.org/10.1038/s41598-018-34709-9> (2018).
- King, M. A. *et al.* Human peripheral blood leucocyte non-obese diabetic-severe combined immunodeficiency interleukin-2 receptor gamma chain gene mouse model of xenogeneic graft-host-like disease and the role of host major histocompatibility complex. *Clin. Exp. Immunol.* **157**, 104–118. <https://doi.org/10.1111/j.1365-2249.2009.03933.x> (2009).
- Torcellan, T. *et al.* In vivo photolabeling of tumor-infiltrating cells reveals highly regulated egress of T-cell subsets from tumors. *Proc. Natl. Acad. Sci. USA* **114**, 5677–5682. <https://doi.org/10.1073/pnas.1618446114> (2017).
- Yu, X. *et al.* Immune modulation of liver sinusoidal endothelial cells by melittin nanoparticles suppresses liver metastasis. *Nat. Commun.* **10**, 574. <https://doi.org/10.1038/s41467-019-08538-x> (2019).

Author contributions

Woo Kyun Bae and Hyun-Jeong Shim concept and design the research. Hyng Jin Bang, Kyung-Hwa Lee, and Myong Suk Park did the research. All authors did the data analysis and interpretation. Hyun Jin Bang, Kyung-Hwa Lee, and Woo Kyun Bae drafted the manuscript. All authors reviewed the critical revision of the manuscript.

Funding

This work was supported by the Bio & Medical Technology Development Program of NRF (NRF-2020M3A9G3080281) and NRF grant (NRF-2020R1A5A2031185) funded by MSIT. Also, this study was supported by a grant (HCRI 22022) Chonnam National University Hwasun Hospital Institute for Biomedical Science.

Competing interests

The authors declare no competing interests.

Additional information

Supplementary Information The online version contains supplementary material available at <https://doi.org/10.1038/s41598-024-69988-y>.

Correspondence and requests for materials should be addressed to H.-J.S. or W.K.B.

Reprints and permissions information is available at www.nature.com/reprints.

Publisher's note Springer Nature remains neutral with regard to jurisdictional claims in published maps and institutional affiliations.

Open Access This article is licensed under a Creative Commons Attribution-NonCommercial-NoDerivatives 4.0 International License, which permits any non-commercial use, sharing, distribution and reproduction in any medium or format, as long as you give appropriate credit to the original author(s) and the source, provide a link to the Creative Commons licence, and indicate if you modified the licensed material. You do not have permission under this licence to share adapted material derived from this article or parts of it. The images or other third party material in this article are included in the article's Creative Commons licence, unless indicated otherwise in a credit line to the material. If material is not included in the article's Creative Commons licence and your intended use is not permitted by statutory regulation or exceeds the permitted use, you will need to obtain permission directly from the copyright holder. To view a copy of this licence, visit <http://creativecommons.org/licenses/by-nc-nd/4.0/>.

© The Author(s) 2024